

Assessment of interatomic potentials for atomistic analysis of static and dynamic properties of screw dislocations in W

D. Cereceda and J. M. Perlado

Universidad Politécnica de Madrid
28005 Madrid, Spain

A. Stukowski, S. Queyreau, and J. Marian*

Lawrence Livermore National Laboratory
Livermore, CA 94551

Lisa Ventelon and M.-C. Marinica

Service de Recherches de Métallurgique Physique, CEA-DEN, F-91191, Gif-sur-Yvette,
France

M. R. Gilbert

EURATOM/CCFE Fusion Association, Culham Science Centre, Abingdon, OX14 3DB,
United Kingdom

E-mail: *marian1@llnl.gov

Abstract. Screw dislocations in bcc metals display non-planar cores at zero temperature which result in high lattice friction and thermally activated strain rate behavior. In bcc W, electronic structure molecular statics calculations reveal a compact, non-degenerate core with an associated Peierls stress ≈ 3 GPa. However, a full picture of the dynamic behavior of dislocations can only be gained by using more efficient atomistic simulations based on semiempirical interatomic potentials. In this paper we assess the suitability of five different potentials in terms of static properties relevant to screw dislocations in pure W. As well, we perform molecular dynamics simulations of stress-assisted glide using all five potentials to study the dynamic behavior of screw dislocations under shear stress. Dislocations are seen to display thermally-activated motion in most of the applied stress range, with a gradual transition to a viscous damping regime at high stresses. We find that one potential predicts a core transformation from compact to dissociated at finite temperature that changes the fundamental energetics of kink-pair production and impacts the mechanism of motion. We conclude that a modified embedded-atom potential achieves the best compromise in terms of static and dynamic screw dislocation properties, although at an expense of about ten-fold compared to central potentials.

1. Introduction.

Tungsten (W) is being considered as a leading candidate for plasma-facing applications in magnetic fusion energy (MFE) devices. The most attractive properties of W for MFE are its high melting point and thermal conductivity, low sputtering yield and low long-term disposal radioactive footprint. These advantages are accompanied unfortunately with very low fracture toughness characterized by brittle trans- and inter-granular failure, which severely restrict the useful operating temperature window [1].

Transgranular plasticity in refractory metals, including W, is governed by the temperature dependence of screw dislocation motion. W is typically alloyed with 5~26 at.% Re to increase low temperature ductility and improve high temperature strength and plasticity [2]. The physical origins behind the Re-induced ductilization have been discussed in the literature [3, 4, 5] and point in some way or another to alterations in the core structure of $\frac{1}{2}\langle 111 \rangle$ screw dislocations, which both reduce the effective Peierls stress σ_P and extend the number of possible slip pathways. A direct consequence of a reduced Peierls stress, *e.g.* as via Re alloying, is an enhanced dislocation mobility at low temperatures. Recent electronic structure calculations of σ_P in pure W give values close to 3 GPa [3]. This means that, under most conditions relevant to technological applications, where stresses are of the order of only a few hundred MPa, a reduction in σ_P of a few hundred MPa may not be significant to the plastic behavior of W and W alloys. Instead, it is the thermally-activated and three-dimensional character of screw dislocation motion, the associated solution softening behavior, as well as the temperature dependence of the core structure, that control bulk ductility.

All of these aspects cannot be studied in atomistic detail using current experimental capabilities. By contrast, atomistic methods based on semiempirical potentials have enabled large-scale molecular dynamics (MD) simulations, so that, at present, calculations of single-dislocation mobility, core structure and transformations, etc., can be obtained with reasonable accuracy. However, care must be exercised when choosing from the dozen or so W potentials available in the literature. Semiempirical force fields with both pair and cohesive contributions (*e.g.* following the EAM formalism) are typically considered to achieve an optimum balance between efficiency and accuracy. These are typically fitted to reproduce some basic bulk and defect properties such as lattice parameter, elastic constants, vacancy formation energy, surface energies, etc., but generally not dislocation properties. Of these, it is known that the screw dislocation core structure at 0K should be non-degenerate (also known as *compact*), as revealed by density functional theory (DFT) calculations [3, 5].

Previous atomistic calculations on screw dislocations in W have been performed by Mrovec *et al* [6], Fikar *et al* [7] and Tian and Woo [8]. Mrovec *et al* studied the dislocation core structure and calculated the Peierls stress at 0K using a tight-binding-based bond-order potential (TB-BOP)[‡]. They predicted a non-degenerate core structure and a Peierls stress of 4.3 GPa. For their part, Fikar *et al* studied core structures and energies of screw dislocations using three different interatomic potentials, all of which display dissociated cores. Lastly,

[‡] BOP potentials include non-central atomic interactions to represent the effect of *d*-electrons in transition metals

Tian and Woo examined the mobility of screw dislocations also with an EAM potential that predicts a dissociated core structure. They were able to obtain dislocation velocities at stresses above the Peierls stress at 0K. However, no systematic study of dislocation motion in W at finite temperature has been conducted. Characterizing dislocation motion in the stress-temperature space is important to parameterize the so-called mobility functions used in higher-level methods such as dislocation dynamics. Mobility functions provide a quantitative measure of the response of dislocations to applied and internal stresses.

Unfortunately, one of the most important difficulties associated with such studies is the scale-dependent nature of MD simulations, which require exceedingly high strain rates to drive the system over time scales accessible computationally, of the order of <1 ns. Because of these limitations, MD is incapable at present of properly capturing the thermally-activated motion of screw dislocations at low stresses. However, MD simulations can still provide valuable input in intermediate-to-high stress conditions and in situations where the deformation rates are high. The objective of this paper is to compare five different interatomic potentials –that have not been fitted against screw dislocation data– and assess their performance in terms of static and dynamic dislocation properties. By static properties we mean several reference screw dislocation parameters at 0K as obtained with DFT calculations. The dynamic behavior is evaluated in terms of screw dislocation mobility as a function of stress and temperature. Due to the absence of ‘reference’ mobility data against which to compare the potentials, we will simply draw several general conclusions based on the intercomparison among potentials.

The paper is organized as follows. First, we discuss the distinctive features of each potential and calculate the structure of a screw dislocation core. The Peierls potential and the γ surface are then calculated and verified against existing DFT and TB-BOP calculations. Subsequently, we introduce the computational setup for the dynamic mobility simulations and calculate dislocation velocities as a function of temperature and stress. Subsequently, a study of the core trajectories in the plane defined by the glide and normal directions is carried out. We finish by analyzing the causes of the temperature-dependent behavior of each potential and emphasizing the insufficiency of static calculations to fully characterize dislocation motion at finite temperatures.

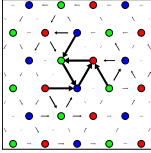
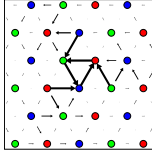
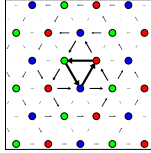
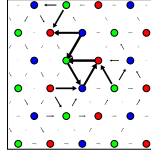
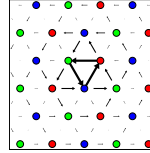
2. Computational details

2.1. Interatomic potentials

Our calculations have been performed with the parallel MD code LAMMPS [14]. Table 1 gives basic information about the five different potentials considered here, among which there are three embedded-atom method (EAM) potentials, one Tersoff-Brenner-type bond-order potential (TF-BOP), and one modified EAM (MEAM). Note that the TB-BOP used by Mrovec *et al* [6] was deemed not suitable for dynamics simulations by its authors [9] and has thus not been considered here. Hereafter they are referred to in the text by the identifiers given in the table header. This selection of W potentials, from the dozen or so available in the

literature, is not meant to be an implicit assessment of the quality of those not employed here.

Table 1. Properties of potentials used. DFT calculations have revealed a Peierls stress $\sigma_P = 2.8$ GPa (0.016μ) and a six-fold symmetric core [3]. W is isotropic elastic and, thus, the value of μ given is equally valid for $\{110\}$ and/or $\{112\}$ slip. The values of the volumetric thermal expansion coefficients, α , are used in Section 3.4. The experimental value for α is 1.45 to $1.91 \times 10^{-5} \text{ K}^{-1}$ in the 1000 to 2000K temperature interval [15].

Potential	EAM1	EAM2	EAM3	TF-BOP	MEAM
Ref.	[16]	[17]	[18]	[19]	[20]
μ (GPa)	160	163	161	170	161
σ_P (μ)	0.025	0.012	0.011	0.006	0.020
Computational cost relative to EAM1	1.0	0.4	0.9	5.4	9.1
Core structure at 0K					
α ($\times 10^{-5} \text{ K}^{-1}$)	1.40	2.42	1.76	2.38	1.64

Two important quantities for characterizing screw dislocation cores at 0K are the Peierls potential, defined as the energy path from one equilibrium position to another on a $\{110\}$ plane, and the γ surface along the $[111]$ also on $\{110\}$ planes. The Peierls energy path has been linked to the morphology of kinks in bcc Fe [21] while Duesbery and Vitek [22] have provided evidence for a direct correspondence between the shape of the $\frac{1}{2}\langle 111 \rangle \{110\}$ gamma surface and the screw dislocation core structure. These are plotted, respectively, for all potentials in Figs. 1 and 2 on the $(1\bar{1}0)$ plane. DFT data for both calculations are also shown for comparison.

The Peierls trajectories were obtained using the nudged elastic band method [23] in the manner proposed by Gröger and Vitek [24], whereas the DFT calculations in both cases were obtained using a *plane wave self-consistent field* code as described in Refs. [25] and [26]. All simulations were run on LLNL’s ATLAS cluster using 128 and 256 processors at a reference cost of $\approx 10^{-9}$ CPU seconds per atom per timestep for potential EAM1.

2.2. Simulation setup

To measure dislocation velocities, we have performed stress-controlled simulations of $\frac{1}{2}\langle 111 \rangle$ dislocations with the maximum resolved shear stress (MRSS) on a $\{112\}$ plane. The justification to focus on $\{112\}$ -type planes is twofold. First, as Argon and Maloof [10] have shown, under tensile loading, most loading orientations and temperatures, result in $\frac{1}{2}\langle 111 \rangle \{112\}$ slip. Also, Li *et al* [5] have shown that $\{112\}$ slip is important in W alloys with

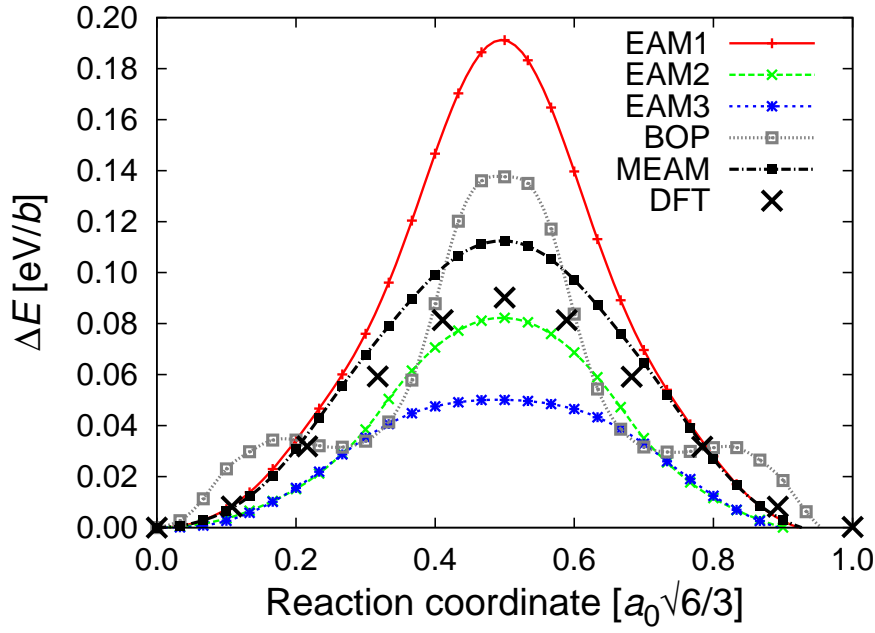


Figure 1. Peierls trajectory for a screw dislocation using all potentials tested here. DFT calculations from Ventelon *et al* [26] are shown for comparison.

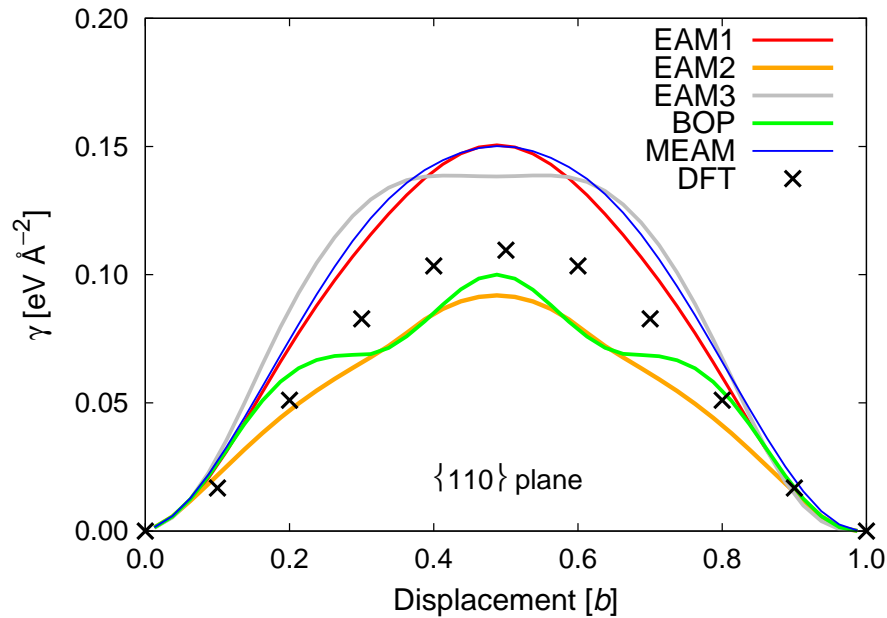


Figure 2. $\{110\}$ γ surface along the $[111]$ direction for all the potentials considered in this work. DFT calculations from Ventelon *et al* [26] are shown for comparison.

high Re concentrations. Second, certain EAM potentials intrinsically deviate from MRSS behavior when the MRSS plane is of the $\{110\}$ type for reasons that have been discussed at length in the literature [11, 30, 12].

We have provided the details regarding the computational setup for this type of simulations in prior publications [12, 13]. Suffice it to say that orthogonal boxes with axes $x \equiv \frac{1}{2}[111]$, $y \equiv [1\bar{1}0]$, and $z \equiv [11\bar{2}]$, corresponding to the line, glide, and plane normal directions, respectively, were used to mitigate finite size effects (cf. Ref. [12]). σ_{xz} is then applied on the computational cell boundaries and simulations are conducted in the npT ensemble. Periodic boundary conditions are used in the line and glide directions. The reference cell dimensions were $L_x = 25 \left[\frac{\sqrt{3}}{2}a_0 \right]$, $L_y = 100 \left[\sqrt{2}a_0 \right]$, and $L_z = 50 \left[\sqrt{6}a_0 \right]$, where a_0 is the lattice parameter (≈ 3.16 Å) and the amounts in brackets are the dimensions of the nominal unit cell in the coordinate system employed here. The reference configuration contains 7.5×10^5 atoms, which results in strain rates of $1.4 \times 10^{6\sim 7} \text{ s}^{-1}$ for dislocation velocities between 10 and 100 $\text{m}\cdot\text{s}^{-1}$.

3. Results

3.1. Raw MD data

The simulation setup, boundary conditions, and velocity calculations, as they relate to the present work, are discussed in depth by Cereceda *et al* [13]. The temperature and stress ranges covered were, respectively, 300 to 2100K and 200 to 2000 MPa. All the simulations were run for 100 ps and configuration data were extracted every picosecond. The procedure to extract dislocation velocities from MD simulations is well established in the literature [27, 28, 12]: from the position of the core, velocities are calculated as the derivative of the displacement-time curves for each case.

3.2. Screw dislocation mobility

Figure 3 shows all the $(\sigma-v)$ data for the five interatomic potentials tested. The figures also contain the temperature dependence for each case. Generally, the velocities increase monotonically with stress and temperature, although at different rates depending on the potential. To first order, the mechanism of motion followed by the dislocations depends on the Peierls stress. This means that, at a maximum applied shear stress of 2000 MPa, the EAM1 and MEAM potentials both operate under σ_P (cf. Table 1), while for the EAM2, EAM3, and TF-BOP there are several data points above it. In either case, dislocation motion is mostly governed by the thermally activated kink-pair nucleation mechanism, and thus display an exponential dependence with σ and T . This can be qualitatively appreciated in the figure.

Another important aspect of dislocation motion is the extent of MRSS motion displayed, *i.e.* whether there are deviations from glide on the MRSS $\{112\}$ -type plane. In Figure 4 we analyze the trajectories on the yz -plane for different combinations of σ and T over 100 ps of simulation. Perfect MRSS behavior is characterized by trajectories parallel to 0° . As the figure shows, all the EAM potentials display nearly perfect MRSS behavior, while for the MEAM small deviations in the acceleration phase are captured. The TF-BOP potential displays the most erratic motion with an overall deviation of the order of five degrees. At

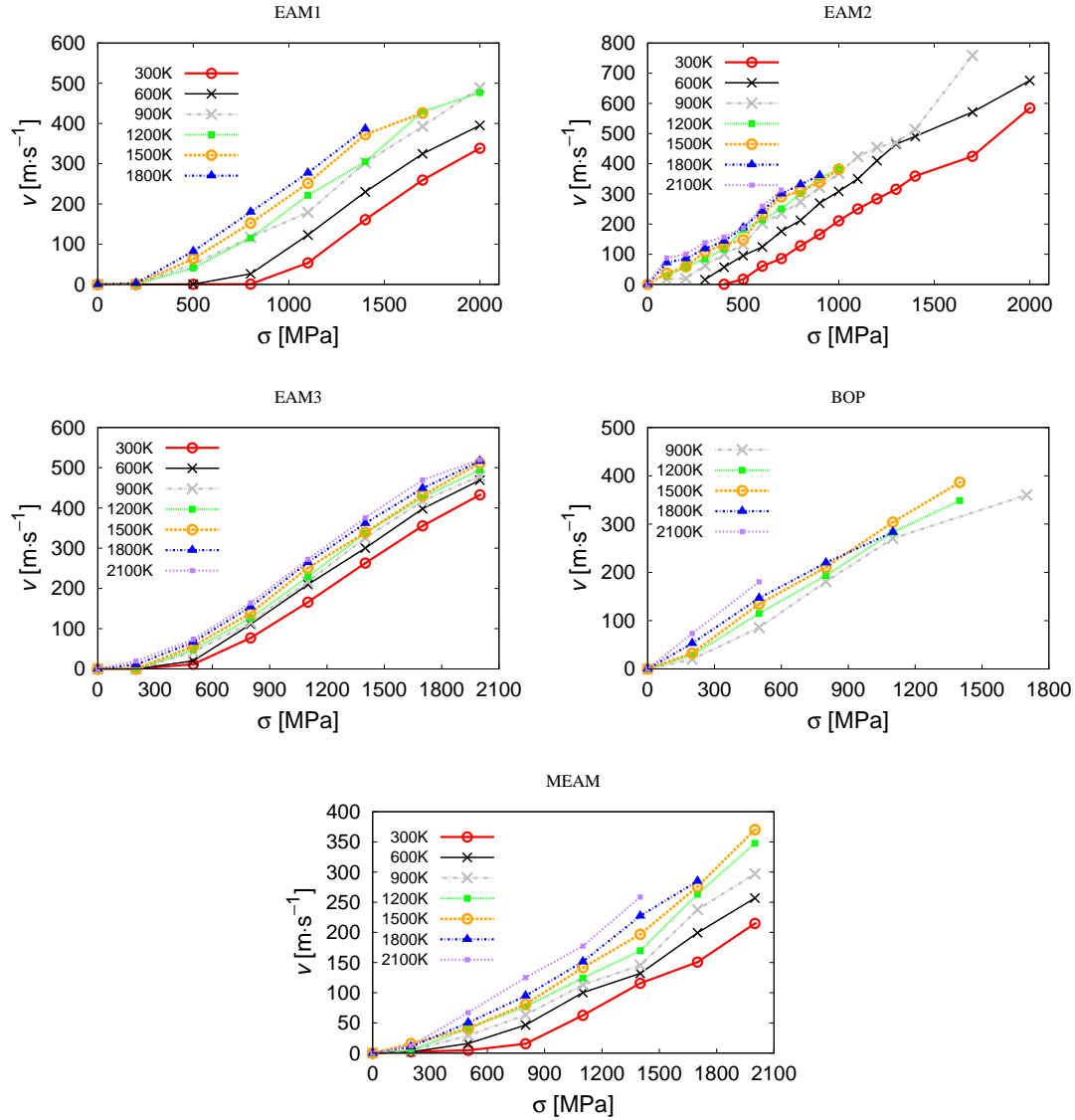


Figure 3. Screw dislocation velocity as a function of applied shear stress and temperature for the five interatomic potentials considered here. Note that the velocity and stress axes are not on the same scale for each case.

higher temperatures and stresses, this effect is enhanced to the point that the dislocation exits the simulation box only a few picoseconds after the shear stress is applied. This is the reason why there are fewer data points in the σ - v curves shown in Fig. 3 for the TF-BOP potential. The trajectories shown in the figure are *effective*, *i.e.* they are not sufficiently time resolved to capture the atomistic details of dislocation motion. Nevertheless, the operating mechanism of motion is by way of nucleation and propagation of kink pairs on $\{110\}$ planes adjacent to the MRSS $(11\bar{2})$ plane.

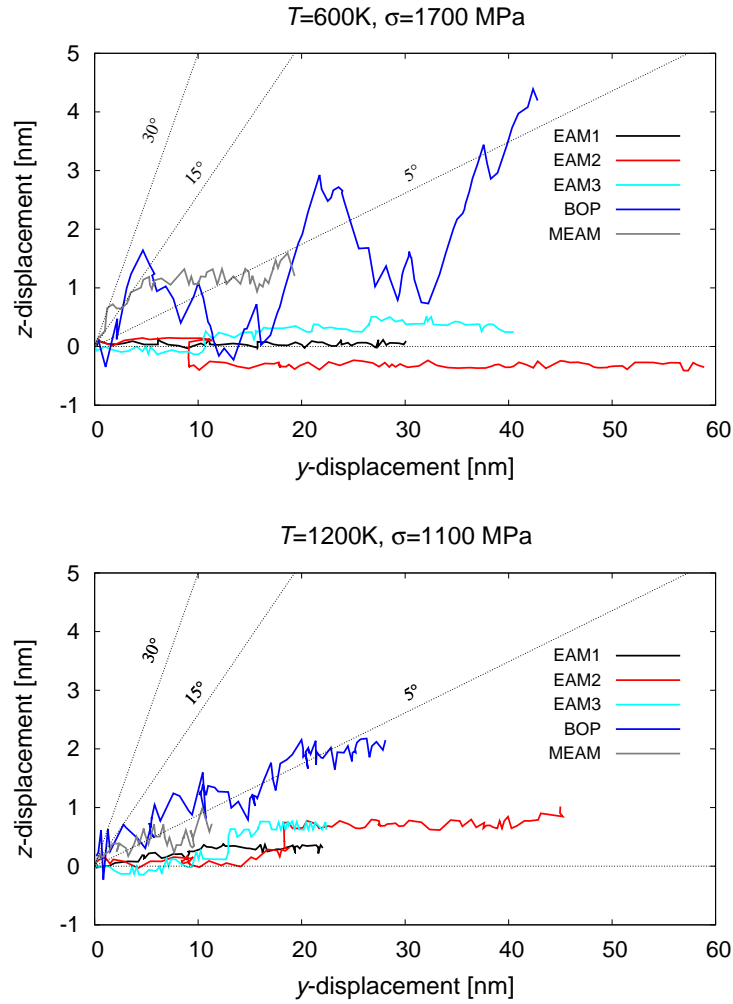


Figure 4. Line-averaged dislocation trajectories on the yz -plane for two combinations of σ and T and over 100 ps. Planes forming 0, 5, 15 and 30° with the $(11\bar{2})$ MRSS plane are represented with dotted lines (angles not to scale). Except for the TF-BOP potential, all the simulations yield small $<5^\circ$ deviations from MRSS motion.

3.3. Dislocation core structure at finite temperature

As shown in Fig. 3, the σ - v data are not conducive to comparison among potentials. Instead, in Fig. 5 they are plotted as a function of interatomic potential for a number of selected temperatures. The figure reveals an interesting trend: the *relative* behavior of all the potentials remains unchanged for all temperatures with the exception of EAM3. At low temperatures, this potential exhibits a relatively high dislocation mobility, akin to that displayed by ‘fast’ potentials such as EAM2. However, above 900K, the mobility is reduced (relative to the other interatomic potentials) to values more in line with ‘slower’ potentials such as EAM1. Moreover, if one examines the trajectories followed by the dislocation at 500 MPa[§], a notable

[§] To be meaningful, this analysis must be performed at relatively low stresses to interfere the least amount possible with the investigated temperature effect.

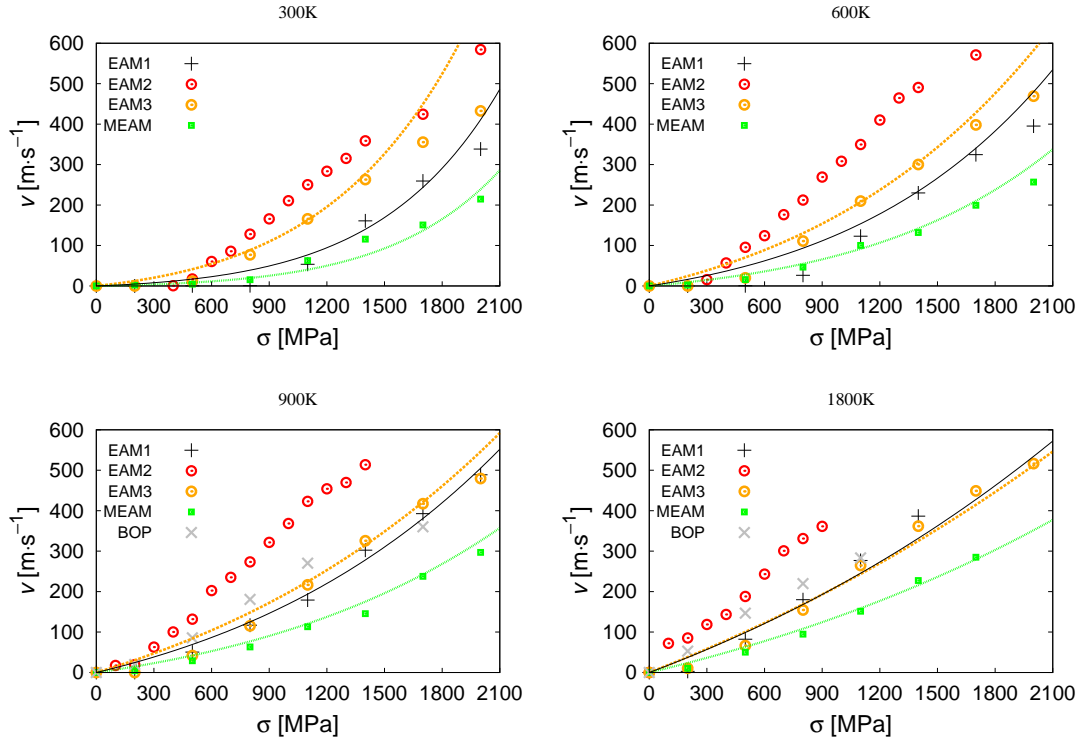


Figure 5. Comparison of interatomic potentials for the data given in Fig. 3. The colored lines correspond to exponential fits obtained in the Appendix for potentials EAM1, EAM3 and MEAM.

difference in behavior within the EAM3 potential can be observed. At a temperature of 600K, the dislocation follows a biased path on an effective glide plane forming $\approx 30^\circ$ with the MRSS plane. However, at 1800K, the dislocation follows a path that deviates only slightly from that dictated by the Peach-Köhler force (*i.e.* 0°). This is quantitatively displayed in Figure 6, where this time the trajectories are resolved with atomistic detail. The figure shows unequivocally that dislocation motion proceeds via the formation of kink pairs on $\{110\}$ planes bordering the MRSS $[11\bar{2}]$ plane (at $\pm 30^\circ$). Moreover, the details of the trajectory at 600K suggest biased formation on the $(10\bar{1})$ plane ($+30^\circ$), whereas at 1800K *random-walk* behavior is displayed, with kink pairs forming equally on both available $\{110\}$ planes.

The behaviors illustrated in Figs. 5 and 6 suggest a change in core structure with temperature for a given stress state^{||}. Moreover, these changes appear to be more acute for potential EAM3 than for the other potentials. To examine the physical structure of the dislocation core at different temperatures one can use time-averaged differential displacement (DD) maps (these maps were used in Table 1 for each 0K configurations). The DD maps are obtained by running MD simulations of crystals containing four screw dislocations arranged in a balanced quadrupole configuration and periodic boundary conditions. The size of the simulation box is $20 \times 15 \times 18$ multiples of the bcc lattice vectors $[111] \times [\bar{1}2\bar{1}] \times [\bar{1}01]$. The dimensions are adjusted to the equilibrium lattice constant at the given temperature.

^{||} We know that stress also induces its own core transformations as explained in Ref. [40].

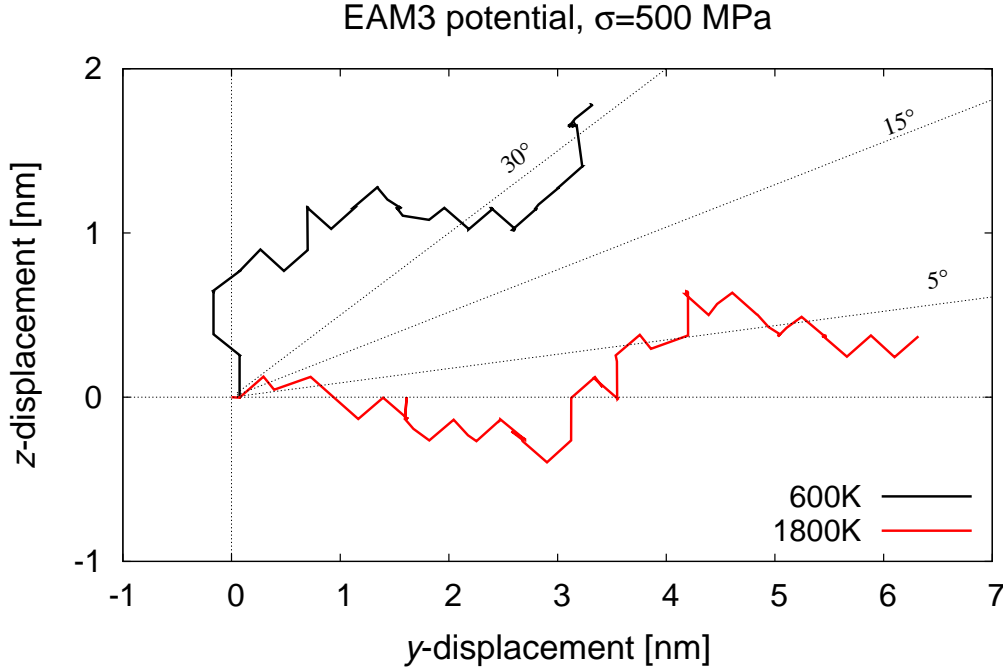


Figure 6. Line-averaged dislocation trajectories on the yz -plane for the EAM3 potential at 500 MPa. Results for two 200-ps temperatures above and below the presumed core transformation temperature of around 1200K are shown. Planes forming 0, 5, 15 and 30° with the $(11\bar{2})$ MRSS plane are represented with dotted lines (angles not to scale).

For the finite temperature simulations, the displacement of each atomic string is determined by averaging over all 40 atoms in the string and over a time window of 100 fs, being sufficiently long to avoid noise due to thermal vibrations yet short enough to not capture diffusive behavior. The results are shown in Fig. 7 for configurations in the $0 < T < 2100\text{K}$ interval. The figure confirms that the the EAM3 core is the only one showing an appreciable transformation from non-degenerate to degenerate, clearly seen at and above 1500K. Although DD maps are a useful tool to quickly analyze core structures, next we complement the results in Fig. 7 with a more quantitative approach based on fundamental lattice properties.

3.4. Analysis of screw dislocation core stability.

Duesbery and Vitek [22] have provided a simple rule that relates the shape of the $\frac{1}{2}\langle 111 \rangle \{110\}$ γ -surface to the core structure at 0K. They used the following inequality:

$$\gamma\left(\frac{b}{3}\right) > 2\gamma\left(\frac{b}{6}\right),$$

to predict whether a screw dislocation will display a compact core. $\gamma\left(\frac{b}{3}\right)$ and $\gamma\left(\frac{b}{6}\right)$ are the energies corresponding to the $\frac{b}{3}$ and $\frac{b}{6}$ magnitudes of the generalized fault vectors, which can be obtained by reference to Fig. 2. The idea is that, if the above inequality is satisfied, $\frac{b}{6}$ -type faults will be preferred over $\frac{b}{3}$ ones, leading to non-dissociated core structures. However,

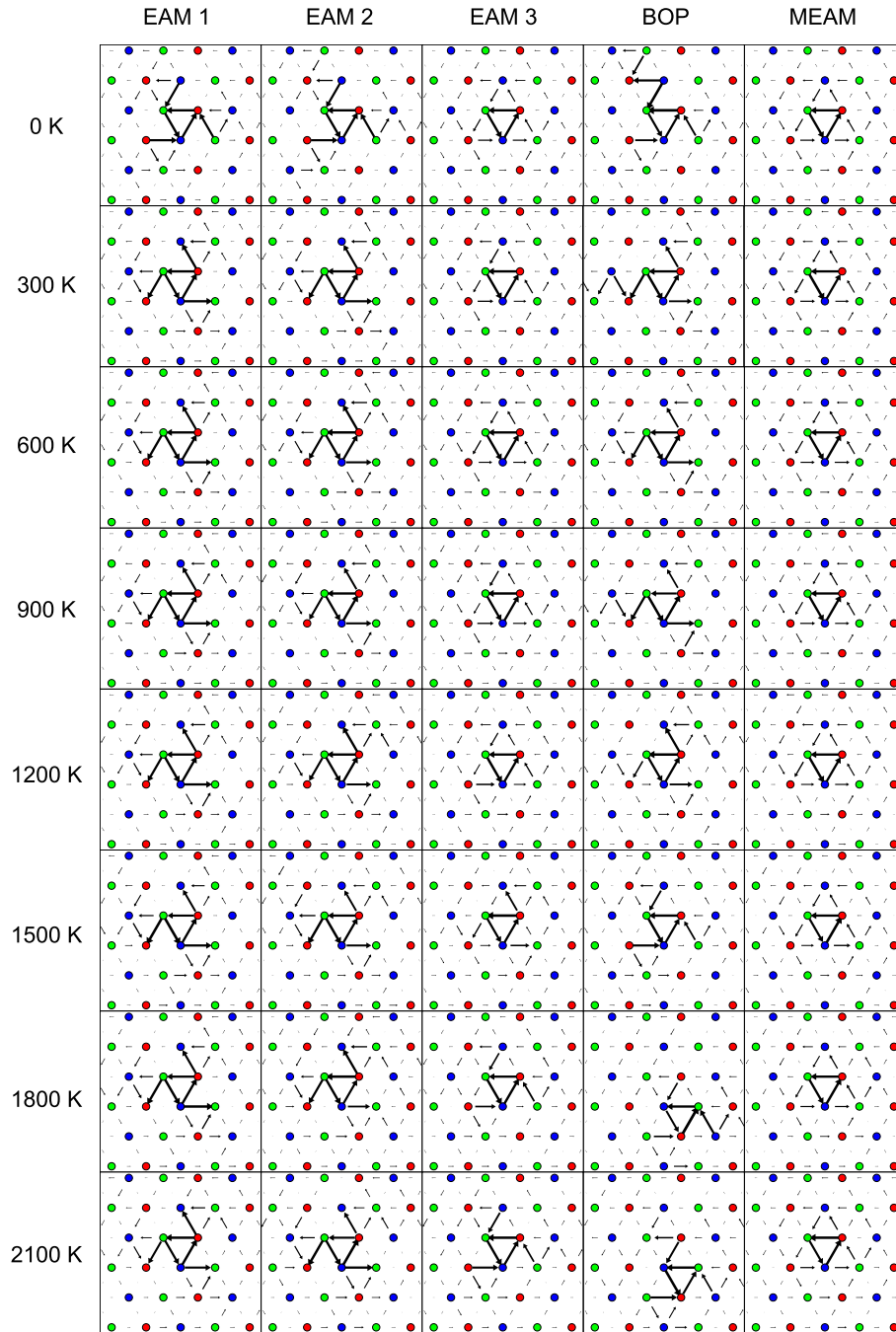


Figure 7. Time-averaged core structures for the five potentials tested here in the entire temperature range.

although Duesbery and Vitek applied this simple rule to six different bcc metals[¶] with remarkable success, we find that in our case it does not hold for potentials EAM1 and EAM2. Thus, here we try a different approach based on the analysis carried out by Gilbert and Dudarev [31].

These authors have shown that, alternatively, the $\frac{1}{2}\langle 111 \rangle$ screw dislocation core structure

[¶] V, Cr, Nb, Mo, Ta, and W, all described by Finnis-Sinclair potentials [41]

in bcc systems can be related to the periodic interaction energy between adjacent $\langle 111 \rangle$ strings of atoms forming the crystal. Their analysis, which was performed primarily to help guide potential development, provides a framework to predict whether the favored core structure at 0K is compact or dissociated. In particular, they derive the so-called “first-nearest-neighbour (1NN) inter-string interaction law” of the potential and use this in a 2D Frenkel-Kontorova (2D-FK) model of interacting $\langle 111 \rangle$ strings to find the minimum energy screw core-structure. Here we extend their methodology to finite temperatures using the quasiharmonic approximation, *i.e.* by relating volume changes to temperature via pre-computed thermal expansion coefficients for each potential. In this fashion, we first compute the inter-string interaction laws as a function of the lattice parameter and then obtain the equivalent temperature as: $T = 3(a/a_0 - 1)/\alpha$. Here, α is the thermal expansion coefficient (given for each potential in Table 1), a_0 the lattice parameter at 0K, and a the lattice parameter corresponding to a temperature T (within the quasiharmonic approximation). For the remainder of this section, we refer to a as $a(T)$ to highlight this temperature dependence.

For each temperature T the 1NN inter-string interaction law $U_1(d)$ was derived by rigidly translating a single $\langle 111 \rangle$ string with respect to a perfect lattice with lattice parameter $a(T)$ and measuring the associated variation in energy under the particular interatomic potential. The resulting curve, which, according to the 2D-FK model defined in Ref. [31], is dominated by the contributions from the moving string interacting with its six 1NNs, can be unfolded using a Fourier analysis to produce the required pair-wise interaction law for the 2D-FK model. An example of such a law for EAM3 at 0K is shown in figure 8(b). A perfect screw dislocation, inserted into a lattice of $\langle 111 \rangle$ atomic strings (for a given $a \equiv a(T)$) according to the isotropic elasticity solution, was then relaxed using $U_1(d)$ and the nature of the relaxed core was determined by visual inspection of its differential displacement map.

Figure 8(a) shows the variation in the favored core structure as a function of T for each of the five potentials. On the y -axis of the plot we have calculated the ratio of the string separation d^* associated with the inflection points in the corresponding $U_1(d)$ law (highlighted by the vertical dotted lines in figure 8(b)) to $b(T)/6$, where $b(T)$ is the corresponding Burgers vector of each potential as a function of T .

As observed by Gilbert and Dudarev [31], the favored core structure depends on the position of the inflection points of the $U_1(d)$ function. Specifically, a fully compact core is characterized by minimum string separations of $b(T)/6$, which are the separation distances in $[111]$ between each of the three $\langle 111 \rangle$ strings immediately surrounding the core (red circles in Figure 8(c), which shows a differential displacement map for a compact core) and their two nearest strings forming the next shell of strings out from the core (blue circles in 8(c)). When the inflection points in $U_1(d)$ are located at a distance of less than or equal to $b(T)/6$, then the compact, non-dissociated core is always stable. Furthermore, even if the separations d^* associated with $U_1''(d) = 0$ are such that $|d^*|$ is somewhat greater than $b(T)/6$, the compact core may still be stable provided that U_1 is only slowly varying around these inflection points—meaning that the forces ($-U_1'(d)$) between strings are relatively constant over a range of d values. This, for example, is the situation in the case of the MEAM potential in figure 8(a), where the ratio $d^*/(b(T)/6)$ is greater than one for all T , but the favored core remains

compact.

However, when the ratio is significantly greater than one, as is the case for both EAM1 and EAM2 at all temperatures, then the compact core becomes unstable and the secondary strings out from the core tend to move towards (along $\langle 111 \rangle$) one of their primary-string neighbors (signified by the major arrows in the “arms” of the non-compact core shown for EAM1 in Table 1) —ultimately leading to the stabilization of the non-compact, three-fold symmetric dissociated core.

Thus, if, as a function of T , there is significant variation in this ratio, then the preferred equilibrium core structure can also change. In our analysis, we find that, consistent with the transition observed in Fig. 7, there is a large shift for EAM3 in the value of $d^*/(b(T)/6)$ (d^* is such that $U_1''(d^*) = 0$) above $\sim 1500\text{K}$. At this point, the equilibrium core structure diverges from the compact core, and becomes more and more dissociated as temperature increases further. In the next section we discuss the implications of our findings.

4. Discussion

4.1. Comparison of static properties of potentials

The five interatomic potentials tested here follow different formulations and have been fitted to different physical properties. It is not our objective to discuss the fitting process or the quality of each one, but only to discuss their performance in relation to screw dislocation modeling. When selecting potentials for screw dislocation simulations, two of the properties most looked at are the core structure and the Peierls stress. For W, these have been obtained using electronic structure calculations by Romaner *et al* [3], which reveal a compact core and $\sigma_P = 2.8\text{ GPa}$. Regarding the core structure at 0K, only EAM3 and MEAM reproduce it correctly, although, as shown in Section 3.3, the EAM3 potential does not preserve this structure at high temperature in what turns out to be a very rich temperature-dependent physical behavior that will be discussed below. In terms of σ_P , the five potentials studied here give a range of values from 1.1 to 4.0 GPa. As Table 1 shows, EAM2 and EAM3 display values just below 2.0 GPa. These potentials are also the most computationally efficient, which is an advantage when computing resources are limited. It is worth noting that the cost of these potentials was evaluated using the cutoff radii specified in the original references shown in Table 1.

Furthermore, the subspace of the energy landscape most relevant to screw dislocation motion is the Peierls trajectory and the γ surface (Figs. 1 and 2). The Peierls trajectory is only correctly reproduced by potentials EAM3 and MEAM, while the rest predict trajectories with metastable states along their path, in disagreement with DFT calculations. Regarding the γ surface, potentials EAM1, EAM3 and MEAM all predict the essential qualitative and quantitative features of the DFT results and are also in good agreement with the results by Gröger *et al* using a TB-BOP [30].

Thus, on the basis of all these calculations, the MEAM potential might be the best suited of those tried here to carry out dislocation simulations, although EAM3 may be a satisfactory

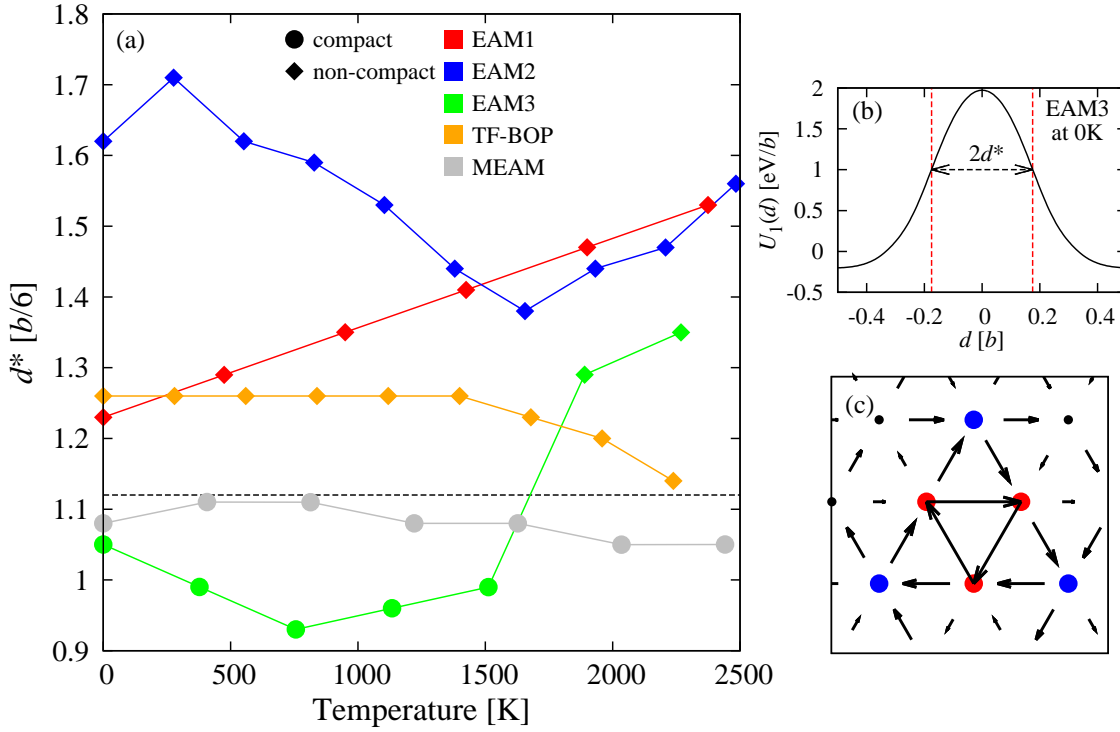


Figure 8. (a) Analysis of the favored core structure for the five different potentials as a function of temperature. A compact core is designated by a circle, and a non-compact by a diamond. The y -position of each point is the magnitude of distance of the inflection points in the 1NN string-interaction law (*i.e.* d^* , which is the distance at which $U_1''(d) = 0$) normalized to the quantity $b(T)/6$, where $b(T) = \sqrt{3}a(T)/2$. The dashed horizontal line separates the region of phase space where compact cores are favored (below) from the region where non-compact are favored (above). (b) The 1NN string-interaction law for EAM3 at 0K. The red dashed vertical lines indicate the position of the inflection points in this curve. (c) Differential displacement map of the compact core predicted at 0K for the U_1 function from EAM3. Each of the three strings closest to the core (red circles) are separated from their two closest secondary strings (blue circles) by $b/6$. In the figure the temperature dependence of b is omitted for the sake of clarity.

replacement at low temperatures and stresses when computational cost is of the essence.

4.2. Mobility of screw dislocations

Dislocation velocities are difficult to infer from straining experiments, while they are costly and subjected to size limitations in simulations. Measurements [34] and calculations [35, 36] of edge dislocation velocities have been carried out in W. However, other than the values computed by Tian and Woo [8] at very high stress (>3.6 GPa), to our knowledge no data exist on screw dislocation mobility in W at low stresses.

A quick look at Fig. 5 reveals several interesting details. First, the EAM2 and MEAM consistently give the highest and lowest velocities, respectively, regardless of temperature. Since atomistic simulations commonly overestimate screw dislocation velocities, particularly in the low-stress range, this may be another reason in favor of using MEAM. This is likely to be due to the fact that the dislocation core remains compact in the entire temperature range using the MEAM potential (cf. Fig. 7). Second, screw dislocations move by thermally-activated mechanisms below the Peierls stress, transitioning to a viscous damping regime above it. At the maximum applied stress of 2000 MPa, some dislocations have been driven past the Peierls stress as given by their respective potentials (cf. Table 1). This is certainly the case for the TF-BOP and possibly potentials EAM2 and EAM3. One would therefore expect to see a gradual exhaustion of the thermally-activated regime and a transition into a linear regime. Interestingly, such a transition appears to occur for potential EAM1 which has $\sigma_P = 4.0$ GPa. It was shown by Gilbert *et al* [12], however, that the actual transition stress decreases with the square of the temperature, which may be what is seen here. Appropriate exponential fits to the data shown in Fig. 5 carried out in the Appendix reveal useful parameters that define the thermally activated regime.

4.3. Dislocation core transformation

The behavior that emanates from the results in Figs. 5 and 6 for potential EAM3 is the manifestation of a temperature-driven dislocation core transformation that occurs as a result of changes to the free energy landscape. The evidence for this transformation comes via differential displacement maps of time-averaged atomic positions at finite temperatures, and a quasiharmonic analysis of the location of inflection points in the $\langle 111 \rangle$ interaction energy, which is known to control the dislocation core structure (cf. Figs. 6 and 8).

This affects the dislocation mobility as well. Dislocation mobility is highly multidimensional in that it displays multiparametric dependencies. Among these, here we have solely focused on dislocation temperature and stress, while we have kept the dislocation character and the slip system constant. We have shown that the reported core transformation has an impact on all of these. Indeed, in a detailed analysis carried out in the Appendix, it is shown that the temperature dependence of fitted σ - v relations at $T < 1200$ K for EAM3 is not carried to higher temperatures. By contrast, the same analysis does not yield significant differences between the low and high temperature regimes for potentials EAM1 and MEAM. This is further indication that the core structure may impact the motion mechanisms in the corresponding temperature range.

4.4. Mechanism of motion

The dislocation trajectories shown in Fig. 6 provide some information about the mechanism of motion when the MRSS plane is of the $\{112\}$ type. Both at 600 and 1800K the dislocation moves by elementary $\{110\}$ kink-pair episodes. However, at high temperature it appears as though the unit mechanism is composed of one $+30^\circ$ jump (on a $(01\bar{1})$ plane) followed by a correlated -30° jump (on a $(10\bar{1})$ plane). In other words, the dislocation appears to move

by kink-pair episodes on the $(11\bar{2})$ plane that consist of two alternating and correlated $\pm 30^\circ$ kinks. This is consistent with the mechanism proposed by Duesbury [37]. Overall, this results in a trajectory that follows a random walk and that, on average, forms zero degrees with the MRSS plane. This is in contrast with the mechanism observed at 600K, where kink pairs on the $+30^\circ$ plane seem to be favored in a proportion of three or more to one over -30° ones. This results in a path that forms $+30^\circ$ on average with the MRSS plane. The effect of the core structure on this behavior is not clear. A mechanism akin to the so-called ‘pencil’ glide could be in effect at 1800K that limits the dislocation core transition pathways.

5. Summary

To summarize, the main findings of this paper can be condensed into the following main items:

- We have calculated static properties relevant to screw dislocations using five different interatomic potentials for W. These include three EAM, one BOP and one MEAM.
- We have calculated screw dislocation mobilities for all potentials on a $\{112\}$ glide plane. Our calculations provide elements to judge the MEAM potential as the most suitable for dislocation calculations.
- We have provided evidence of a new physical mechanism by which the screw dislocation core suffers a transformation from compact to dissociated at some finite temperature. This occurs only for one of the tested potentials.
- This transformation does impact dislocation mobility, showing once more that, first, the atomistic nature of the dislocation core governs behavior at larger scales and, second, a purely static treatment of the dislocation core is insufficient to predict and describe the dynamics of dislocations.

Acknowledgments

This work was performed under the auspices of the U.S. Department of Energy by Lawrence Livermore National Laboratory under Contract DE-AC52-07NA27344. We specifically acknowledge support from the Laboratory Directed Research and Development Program under project 11-ERD-023. D.C. and J.M.P. acknowledge support from the 7th Framework Programme with project HiPER: European High Power Laser Energy Research Facility, Grant Agreement No. 211737. We specifically acknowledge the PhD program support from Universidad Politécnica de Madrid. This work was also partly funded by the RCUK Energy Programme under grant EP/I501045 and the European Communities under the contract of Association between EURATOM and CCFE. The views and opinions expressed herein do not necessarily reflect those of the European Commission.

Appendix A.

Here we analyze the overall impact of the dislocation core transition for potential EAM3 on dislocation mobility. We fit the data given in Fig. 3 to the general expression:

$$v(\sigma, T) = A\sigma \exp\left(-\frac{H_0 - \sigma V^*}{kT}\right) \quad (\text{A.1})$$

where A , H_0 , and V^* are fitting constants that represent, respectively, a velocity prefactor, the kink pair energy at 0K, and the activation volume. We obtain these for three potentials, namely, EAM1, EAM3, and MEAM, and carry out the fit first including all temperatures. The results for each case are shown in Table A1. These values deserve some commentary,

Table A1. Fitting parameters for the analytical mobility function A.1. The average fitting error for A , H_0 , and V^* was, respectively, 6, 9 and 10%. Regular script: values from full temperature fits; bold script: values from low temperature ($\leq 900\text{K}$) fits; in parentheses: percentage difference between both sets of fits.

Potential	A [$\text{ms}^{-1}\text{MPa}^{-1}$]	H_0 [eV]	V^* [b^3]
EAM3	0.26 0.24 (8%)	0.05 0.04 (20%)	0.42 0.19 (55%)
MEAM	0.19 0.17 (10%)	0.08 0.07 (12%)	0.26 0.23 (12%)
EAM1	0.30 0.28 (7%)	0.08 0.07 (12%)	0.24 0.24 (0%)

particularly H_0 and V^* . Using the method described by Ventelon and Willaime [25], we have obtained a kink-pair energy of $H_0 = 1.7$ eV for the MEAM potential. Experimentally, Brunner [42] has obtained a value of 1.75 eV from the temperature dependence of flow stress measurements in W, in very good agreement with the calculated value but significantly higher than the MD values. Giannattasio *et al* [43] have obtained values of the order of 1.0 eV inferred from the strain rate dependence of the brittle-to-ductile transition, still much larger than those reported here. Similarly, Tarleton and Roberts [44] have found values of $V^* = 20b^3$ to be representative of the kink-pair process in W. Again, these are two orders of magnitude larger than ours. The magnitudes of H_0 and V^* obtained in our analysis suggest a very ‘soft’ thermally activated process, something not necessarily consistent with the static data presented in Section 2.1. The low values of H_0 and V^* obtained in our simulations are likely due to overdriven screw dislocation dynamics in the MD simulations.

Next, we obtain additional fits using only data at 300, 600, and 900K, *i.e.* at temperatures below the presumed core transformation for potential EAM3. The corresponding parameter values are shown in bold script for each case in Table A1. The percentage difference between the values for full and low temperature fits is given in parentheses. Although the differences in the parameter A are similar in all cases, those for H_0 and V^* are clearly largest for EAM3. Particularly, the differences in the activation volume, which is known to be most sensitive to the core structure, are considerable. This further reinforces the notion that, from a dynamical standpoint, dislocations are behaving differently below and above $\approx 1000\text{K}$. In contrast, for the other two potentials, the dynamic behavior above and below this presumed transition

temperature is governed by the same laws. The low temperature fits obtained here are shown in Fig. 5. The fits provide very good agreement with the EAM1 and MEAM data at all temperatures, whereas they gradually worsen for EAM3 as temperature increases. As well, the deviation of the fits above σ_P for potential EAM3 can be clearly appreciated.

- [1] S. J. Zinkle and N. M. Ghoniem, *Journal of Nuclear Materials* **417**, 2 (2011).
- [2] E. Lassner and W. F. Schubert, *Tungsten: Properties, Chemistry, Technology of the Element, Alloys, and Chemical Compounds* (Kluwer Academic/Plenum Publishers, New York, NY, 1999).
- [3] L. Romaner, C. Ambrosch-Draxl, and R. Pippan, *Physical Review Letters* **104**, 195503 (2010).
- [4] S. Wurster, B. Gludovatz, and R. Pippan, *International Journal of Refractory and Hard Materials* **28**, 692 (2010).
- [5] H. Li, S. Wurster, C. Motz, L. Romaner, C. Ambrosch-Draxl, and R. Pippan, *Acta Materialia* **60**, 748 (2012).
- [6] M. Mrovec, R. Gröger, A. G. Bailey, D. Nguyen-Manh, C. Elsässer, and V. Vitek, *Physical Review B* **75**, 104119 (2007).
- [7] J. Fikar, R. Schaublin, and C. Björkas, *Advanced Materials Research* **59**, 247 (2009).
- [8] X. Tian and C. Woo, *Materials Science and Engineering A* **369**, 210 (2004).
- [9] M. Mrovec. Private communication.
- [10] A. S. Argon and S. R. Maloof, *Acta Metall.* **14**, 1449 (1966).
- [11] J. Chaussidon, M. Fivel, and D. Rodney, *Acta Materialia* **54**, 3407 (2006).
- [12] M. R. Gilbert, S. Queyreau, and J. Marian, *Physical Review B* **84**, 174103 (2011).
- [13] D. Cereceda, J. M. Perlado, and J. Marian, *Comp. Mater. Sci.* **62**, 272 (2012).
- [14] S. J. Plimpton, *J. Comp. Phys.* **117**, 1 (1995).
- [15] R. H. Knibbs, *J. Sci. Ins.* **2**, 515 (1969).
- [16] X. W. Zhou and *et al.*, *Acta Materialia* **49**, 4005 (2001).
- [17] G. J. Ackland and R. Thetford, *Philosophical Magazine A* **56**, 15 (1987).
- [18] This potential was fitted in the same fashion as the M07 potential for Fe given in Ref. [38]. The potential is based on the force matching method of Ercolessi-Adams [39] and includes fitting data from two main sources. The first includes perfect crystal experimental properties, such as the lattice constant and the elastic constants. The second source includes DFT-calculated defect properties as well as force fields associated with several liquid W configurations. Using this procedure, several converged sets of parameters are produced, but only those parameterizations yielding the desired dislocation properties are retained.
- [19] N. Juslin, P. Erhart, P. Träskelin, J. Nord, K. O. E. Henriksson, K. Nordlund, E. Salonen, and K. Albe, *J. Appl. Phys.* **98**, 123520 (2005).
- [20] H. Park, M. R. Fellingner, T. J. Lenosky, W. W. Tipton, D. R. Trinkle, S. P. Rudin, C. Woodward, J. W. Wilkins, and R. G. Hennig, *Physical Review B* **85**, 214121 (2012).
- [21] P. A. Gordon, T. Neeraj, Y. Li, and J. Li, *Modelling Simul. Mater. Sci. Eng.* **18**, 085008 (2010).
- [22] M. S. Duesbery and V. Vitek, *Acta Materialia* **46**, 1481 (1998).
- [23] G. Henkelman, G. Johansson, and H. Jonsson, *Progress on Theoretical Chemistry and Physics* (Kluwer, 2000), pp. 269–300.
- [24] R. Gröger and V. Vitek, *Modelling Simul. Mater. Sci. Eng.* **20**, 035019 (2012).
- [25] L. Ventelon and F. Willaime, *J. Comp.-Aided Mater. Des.* **14**, 85 (2007).
- [26] L. Ventelon and F. Willaime, unpublished.
- [27] V. V. Bulatov and W. Cai, *Computer Simulation of Dislocations* (Oxford University Press, Oxford, UK, 2008).
- [28] D. L. Olmsted, L. G. Hector, W. A. Curtin and R. J. Clifton, *Modelling Simul. Mater. Sci. Eng.* **13**, 371 (2005).
- [29] J. A. Zimmerman, C. L. Kelchner, P. A. Klein, J. C. Hamilton, and S. M. Foiles, *Physical Review Letters* **87**, 165507 (2001).
- [30] R. Gröger, V. Racherla, J. L. Bassani, and V. Vitek, *Acta Mater.* **56**, 5412 (2008).
- [31] M. R. Gilbert and S. L. Dudarev, *Philosophical Magazine* **90**, 1035 (2010).
- [32] G. M. Torrie and J. P. Valleau, *Chem. Phys. Lett.* **28**, 578 (1974).
- [33] C. H. Bennett, *J. Comp. Phys.* **22**, 245 (1976).
- [34] H. W. Schadler, *Acta Metallurgica* **12**, 861 (1964).
- [35] P. Gumbsch and H. Gao, *Science* **283**, 965 (1999).

- [36] Q. Li and S.-Q. Shi, *Applied Physics Letters* **80**, 3069 (2002).
- [37] M. S. Duesbery, unpublished work.
- [38] L. Malerba, M. C. Marinica, N. Anento, C. Björkas, H. Nguyen, C. Domain, F. Djurabekova, P. Olsson, K. Nordlund, A. Serra, et al., *J. Nucl. Mater.* **406**, 19 (2010).
- [39] F. Ercolessi and J. B. Adams, *Europhysics Letters* **26**, 583 (1994).
- [40] D. Rodney and L. Proville, *Phys. Rev. B* **79**, 094108 (2009).
- [41] M. W. Finnis and J. E. Sinclair, *Philos. Mag. A* **50**, 45 (1984).
- [42] D. Brunner, *Mater. Trans. JIM* **41**, 152 (2000).
- [43] A. Giannattasio, M. Tanaka, T. D. Joseph, and S. G. Roberts, *Phys. Scr.* **T128**, 87 (2007).
- [44] E. Tarleton and S. G. Roberts, *Philosophical Magazine* **89**, 2759 (2009).